Journal of Materials Chemistry A

PAPER

View Article Online
View Journal | View Issue

CrossMark click for updates

Cite this: J. Mater. Chem. A, 2016, 4, 7060

The formation mechanism of Janus nanostructures in one-pot reactions: the case of Ag–Ag_8GeS_6†

Joel van Embden,*[a] Laure Bourgeois,[bd] Enrico Della Gaspera,[a] Lynne Waddington,[c] Yuefeng Yin,[d] Nikhil V. Medhekar,[d] Jacek J. Jasieniak[d] and Anthony S. R. Chesman*[c]

Received 15th January 2016
Accepted 10th March 2016

DOI: 10.1039/c6ta00398b

www.rsc.org/MaterialsA

Herein we describe a large-scale, non-injection "one-pot" batch method for producing large quantities of novel colloidal Ag–Ag_8GeS_6 heteronanostructures. Using a suite of analytical techniques, including high resolution TEM, HAADF-STEM, XEDS mapping, and XRD, the formation mechanism of the nanostructures is elucidated. The formation is discovered to occur in three stages comprising nucleation, phase separation of the metal and semiconductor components, and the final segregation of the metal and semiconductor components to form the Janus nanostructure. The high ionic mobility and chemical reactivity of Ag enables the self-regulated formation of Janus nanostructures in optimized one-pot reactions – a phenomenon that is almost unique to silver-based systems. As such, silver-based systems are ideal candidates to study the formation of Janus nanostructures.

Published on 08 April 2016. Downloaded by Monash University on 5/27/2024 4:09:11 AM.

Introduction

Janus nanostructures are a subclass of heteronanostructures that specifically comprise two material types (and regions) that are bonded adjacently into a single particle. The combination of the two materials in these nanostructures can be tailored specifically to give rise to a synergistic effect, resulting in a substantial increase in their desired efficacy compared to the use of their individual component materials without such intimate physical contact.[1–4] In light of this, they have found use in a broad range of areas, including energy-based applications,[5] plasmonics,[6] and catalysis.[7,8]

Of particular interest are Janus nanostructures that comprise a metal and a semiconductor component. By carefully selecting different material combinations, the resultant Mott–Schottky heterojunction at the interface between the two components may be tailored to favour the rapid transfer of electrons or holes (charge separation) between the metal and the semiconductor. In their high-energy charge separated state these structures may be employed to drive chemical transformations,[9–11] or to modulate conduction within nanoelectronic photoconductive devices.[12,13] The unique ability to tailor the energy levels to suit their application, coupled with their high surface area, makes colloidal metal–semiconductor Janus nanostructures particularly attractive as photoactive materials.[14]

Fuelled by the continuing desire to exploit their distinctive physical and electronic properties, over the past several years numerous reports have outlined the synthesis of a variety of colloidal heteronanostructures.[3–6,15–25] The formation of colloidal heteronanostructures is known to occur through a variety of routes. The most widely adopted method is heterogeneous deposition of secondary components onto seed nuclei.[26–33] However, diffusion-based segregation of multicomponent nanoparticles,[34,35] and ion exchange within a template particle[33,36,37] are also established techniques.

Despite knowledge of such mechanisms, a large number of reports on colloidal heteronanostructures focus solely on either the preparation and characterization or application of novel materials without providing an in-depth analysis of how the structures were formed. This is likely a consequence of the fact that, as detailed above, the vast majority of reports outline the synthesis of heteronanostructures using a seeded growth method (discrete sequential synthetic steps), which makes their formation pathways rather intuitive. Uncovering the formation mechanism is far more difficult to accomplish when the nanostructures are produced in a single step (one-pot) reaction. This may be attributed to the extensive characterization required to effectively decouple the dynamic transformations that occur in solution. In fact, only a few systems are amenable to heterostructure formation in one-pot reactions, which require a highly diffusive component (atomic species) to drive the required phase separation. In light of these factors, investigations that have contributed to the understanding of the underlying formation mechanism of colloidal Janus nanostructures in single-step reactions are rare.[35,38–43]

[a]School of Science, RMIT University, Victoria 3001, Australia. E-mail: joel.vanembden@rmit.edu.au

[b]Monash Centre for Electron Microscopy, Monash University, Victoria 3800, Australia

[c]CSIRO Manufacturing, Bayview Ave, Clayton, Victoria 3168, Australia. E-mail: anthony.chesman@csiro.au

[d]Department of Materials Science and Engineering, Monash University, Victoria 3800, Australia

† Electronic supplementary information (ESI) available: Additional HRTEM images, X-ray diffraction patterns, and optical modelling. See DOI: 10.1039/c6ta00398b

This journal is © The Royal Society of Chemistry 2016

Published on 08 April 2016. Downloaded by Monash University on 5/27/2024 4:09:11 AM.

Silver-based systems hold a special appeal for researchers investigating the formation of colloidal heteronanostructures. The high ionic mobility and chemical reactivity of the Ag^+ cation enables facile solid–solid phase separation into nanostructured components. These properties have been exploited to form a suite of silver-based heteronanostructures.[35,36,38,41–47] In the continued search for novel materials Ag_8GeS_6 (argyrodite) has recently garnered the attention of researchers as its bulk band gap of ~1.4 eV [49] makes it ideal as a broad-spectrum absorber material for both photocatalytic[48] and photovoltaic devices.[49] As such, the properties of Ag_8GeS_6 make it ideal for further exploitation by incorporation into a Janus nanostructure.

Here we outline for the first time the synthesis and characterization of Ag–Ag_8GeS_6 Janus nanostructures with a specific focus given to their formation mechanism. Using a suite of analytical techniques, we track the complex compositional, morphological, and optical changes that occur during the formation process. Uncovering such transformation mechanisms by rigorous investigation is fundamental to progress the development of Janus nanostructures in general. Consequently, we expect that, in addition to providing specific insights into the Ag–Ag_8GeS_6 system, the synthetic chemistry and detailed formation mechanisms elucidated herein provide a broader platform to rationally tailor the synthesis of as yet unexplored Janus metal–semiconductor materials of varying types and compositions.

Experimental

Materials

Silver acetate, Ag(OAc) (99%), dodecanethiol (DDT) (98%), GeO_2 (99.99%), glycolic acid ($GlyH_2$) (99%), and technical grade oleylamine, OLA (70%) were purchased from Aldrich. Carbon disulphide, CS_2 (99.9%), chloroform (99.8%), EtOH (99.5%) and MeOH (99.8%) were purchased from Merck. All reagents and solvents were used as received without further purification. $[Ge(gly)_2(H_2O)_2]$ was prepared according to a previously established literature synthesis.[50]

Synthesis of Ag–Ag_8GeS_6 Janus nanostructures

Ag(OAc) (2.124 g, 12.7 mmol) and $[Ge(gly)_2(H_2O)_2]$ (0.818 g, 3.2 mmol) were suspended in a 4 : 3 (v/v) OLA/DDT solution (56 ml) and heated with stirring to 120 °C under vacuum (*ca.* 1×10^{-1} mbar). Over a period of 30 min the reaction solution was degassed and the reactants dissolved to give a transparent, yellow/green coloured reaction solution. At the conclusion of the degassing step, the reaction solution was cooled to room temperature in an ice bath, resulting in the formation of a white slurry. The solution was then placed under an atmosphere of N_2. Once the solution temperature decreased below 10 °C a solution of DDT (8 ml) and CS_2 (600 μl, 10.0 mmol) was added slowly (over 5 min) with stirring, causing the slurry to change to a light yellow colour, indicating the formation of metal dithiocarbamate species in solution.[38] The reaction solution was then placed under vacuum again (*ca.* 5.0×10^{-2} mbar) resulting in vigorous degassing. Once the solution was stable under vacuum it was then heated over a 10 min period to 100 °C. Upon heating the colour of the solution turned dark brown/black at ~45 °C. After degassing at 100 °C for 30 min, the reaction solution was placed under an atmosphere of nitrogen and heated to 220 °C over a 10 min period, with the temperature then being maintained for a further 20 min. The reaction vessel was then removed from the heating mantle and allowed to cool naturally to room temperature. This method typically yielded between 2 and 2.5 g of product.

Time-dependent aliquots

To investigate the formation mechanism of the colloidal nanostructures small (~1 ml) aliquots were removed by using a syringe through a septum at various temperatures during the heat-up step of the reaction. Notably, the 100 °C aliquot was taken at the conclusion of the second degassing step and used for analysis (N.B an aliquot taken at the beginning of the second degas step had a near identical absorption spectrum to the sample removed at the conclusion of this step). All samples were purified by numerous precipitation/dispersion cycles from chloroform/methanol.

Transmission electron microscopy (TEM) grid preparation

To obtain highly pure samples appropriate for high-resolution imaging and analysis a small portion of each of the washed samples in chloroform was centrifuged at 12 000 rpm for 10 min to obtain a plug of pure particles. Care was taken to ensure that no size selection was performed at any stage during the purification procedure. These highly pure samples were then used for all the TEM experiments.

Instrumentation

UV-vis-NIR absorption spectra were collected at room temperature using a Varian Cary 5 spectrophotometer. X-ray diffraction (XRD) was performed on a Bruker D8 diffractometer equipped with a Cu-Kα radiation source and operated at 40 mV and 40 mA. Low resolution TEM (LRTEM) was performed on a FEI Tecnai 12 G2 transmission electron microscope operating at 120 keV. Images were recorded using a MegaView III CCD (Olympus, Tokyo). High-resolution TEM (HRTEM) was performed using a JEOL JEM 2100F field-emission gun instrument operated at 200 kV, equipped with a Gatan Ultrascan 1000 CCD camera. The JEOL 2100F microscope has a point resolution of <2.3 Å. X-ray energy dispersive spectroscopy (XEDS) was carried out in scanning transmission electron microscopy mode using a JEOL Si(Li) 50 mm^2 detector. The XEDS maps were obtained in two ways: (1) by collecting ~200 frames 256 × 256 in size with a dwell time of 0.2 ms per pixel and drift correction using JEOL's JDS software; (2) in spectrum imaging mode *via* Gatan Digital-Micrograph, with typical acquisition times of 3–4 s per point, a pixel size of 5–7 Å and drift correction. The STEM images were collected in high-angle annular dark field (HAADF) and bright field (BF) modes. The Fast Fourier Transforms of HRTEM images were performed in Gatan Digital Micrograph using a spherical mask to minimise shape effects. The *in situ* heating experiment employed a Gatan 652 tantalum furnace heating holder.

Published on 08 April 2016. Downloaded by Monash University on 5/27/2024 4:09:11 AM.

Results and discussion

Synthesis and characterization

The nanostructures prepared herein were synthesized using a dual precursor heat-up methodology.[51] This general method permits the synthesis of large quantities of nanomaterial with tight size distributions without precursor injection.[52] Our reaction scheme employed both highly reactive silver dithiocarbamate species and our recently developed air and moisture stable $Ge(gly)_2(OLA)_2$ species to ensure the rapid nucleation of nanocrystals at low temperatures.[50] Further growth was afforded through the decomposition of DDT at higher temperatures.

To elucidate the crystal structure of the as-prepared particles and determine their phase purity, XRD was performed. Fig. 1A shows the XRD pattern of the purified particles, which matches perfectly to the expected reflections of orthorhombic argyrodite Ag_8GeS_6 (ICDD# 44-1416). Fig. 1B shows a representative transmission electron microscope (TEM) image of the purified colloidal product at the end of the assigned 20 min growth period. The particles are seen to be quite uniform in size and show a pyramidal morphology, with almost all of the particles displaying a single hemi-spherical protrusion on either one of the vertices (blue circle) or faces (pink circle). The average size of the particles (edge length) is 10.9 ± 2.8 nm with a calculated numerical standard deviation of 19.2% (*vide infra*).

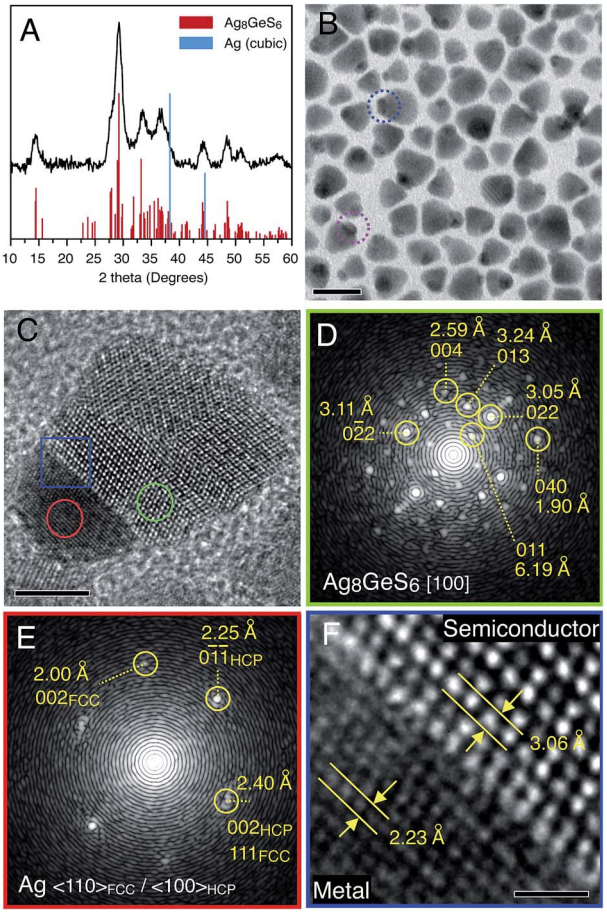

Fig. 1 (A) X-ray diffraction pattern of the final as-prepared nanocrystals. The reflections are seen to match perfectly to Ag_8GeS_6 (ICDD# 44-1416). (B) TEM image of the final isolated nanocrystals. Scale bar 20 nm. (C) HRTEM image of a single particle clearly showing the two components of the nanostructure. Scale bar 5 nm. (D & E) FFT images from the masked areas of the single particle highlighting the metal (red) and semiconductor (green) components. (F) HRTEM image highlighting the epitaxial interface between the two materials (blue box). Scale bar 1 nm.

HRTEM was conducted in order to characterize each of the observed structural components within the nanocrystals. Fig. 1C shows a HRTEM image of a single highly crystalline particle. The darker component is larger than that typically observed within the final sample, but this nanoparticle was chosen to aid in the analysis of the particle structure. From simple visual inspection this "dark" region is seen to have a radically different crystal structure compared to the bulk of the particle. Furthermore, the obvious difference in the scattering intensities (for samples of similar thickness) is indicative of elements with different atomic masses and materials with very different atomic number densities. Clear twinning is observed in the larger bulk particle while the darker component appears to be a single crystal.

To determine the crystal structure of each of these two components selected area Fast Fourier Transformation (FFT) was performed. An area of each component was masked (red and green circles) and used to generate FFT images. The FFT image of the lattice from the bulk of the particle is indicative of a highly complex and intricate crystal structure (green circle; Fig. 1D). Nevertheless, all spots could be readily indexed to the [100] zone axis of Ag_8GeS_6. In contrast, the FFT image of the protrusion displays multiple disparate lattice spacings, all of which are consistent with metallic silver (Fig. 1E). Specifically, the spots at 2.00 Å and 2.40 Å may be readily assigned to the interplanar spacings of the (002) and (111) lattice planes of face centred cubic (FCC) silver, respectively, and correspond to a ⟨110⟩ oriented FCC Ag crystal. An additional dominant spacing at 2.25 Å is also observed, which may be indexed to the (011) lattice plane of ⟨100⟩ oriented hexagonal close packed (HCP) Ag. Although it is unusual to observe HCP and FCC spots in the same FFT image, hexagonal regions have previously been observed within FCC Ag nanocrystals that are highly disordered.[53,54] Analysis of multiple particles revealed that, in contrast to the large relatively crystalline Ag component displayed in Fig. 1C, in a large number of cases the Ag component was smaller and either multiply twinned or highly disordered‡ (see ESI; Fig. S1†).

The general observation of disorder and twinning in the Ag lattice explains the absence of a clear FCC Ag reflection in the XRD pattern. Such irregularities in the lattice significantly reduce the domain size, which broadens the reflections, making them difficult to detect in regions where argyrodite peaks are

‡ Given the high solubility of germanium in silver,[71] at this juncture we cannot rule out that the small perturbations to the FCC lattice parameters and the disorder are not a result of trace Ge incorporation. However, twinning in Ag lattices is commonly observed. Furthermore, we submit that the extent of disorder in these structures may arise simply as a consequence of the rapid diffusion induced phase separation (*vide infra*).

This journal is © The Royal Society of Chemistry 2016

Published on 08 April 2016. Downloaded by Monash University on 5/27/2024 4:09:11 AM.

present. However, it is also important to note that the XRD pattern of analogous structures of Ag–Ag_8SnS_6 did not display cubic silver, despite a highly crystalline metal (Ag) domain.[47] Fig. 1F (blue box) shows the epitaxial nature of the interface between the two material types with clear differences in the lattice spacing between the metal (2.23 Å; [011]) and the semiconductor (3.06 Å; [022]) components. Collectively, these data confirm that the as-prepared particles are metal–semiconductor Janus nanostructures of the type Ag–Ag_8GeS_6.

Formation mechanism of Ag–Ag_8GeS_6 heteronanostructures

Herein we focus on the formation of Ag–Ag_8GeS_6. To elucidate the formation mechanism of these Janus nanostructures, time-dependent aliquots were taken during the heat-up process. Fig. 2 shows TEM images and the corresponding particle size distributions (PSDs) of the particles at temperatures between 100 °C and 220 °C, highlighting the change to the morphology of the particles during the heat-up stage of the reaction. It can be seen clearly that at 100 °C the particles are highly monodisperse and have already grown to a size of 7.5 nm. Little change in the morphology is seen with further heating to 140 °C, although dark patches are observed in the centres of some of the particles. Intriguingly, by 180 °C all of the particles are seen to display a core/shell structure with a strongly electron diffracting core of 3–4 nm in size. At 220 °C the particles have become less spherical and the strongly electron diffracting regions now appear on the sides of the particles. Further heating (20 min) at 220 °C results in a massive change in morphology with the overall particle shape becoming pyramidal, with each particle having a singular hemispherical protrusion attached to either the edge or the vertex of the main crystal. Inspection of the PSDs during heat-up reveals that there is very little change to the overall particle size during the heat-up stage (7.5 to 8.2 nm; as highlighted by the vertical dotted line). However, after 20 min of heating at 220 °C the particles undergo significant growth to 10.9 nm (edge length) accompanied by a broadening of the PSD.

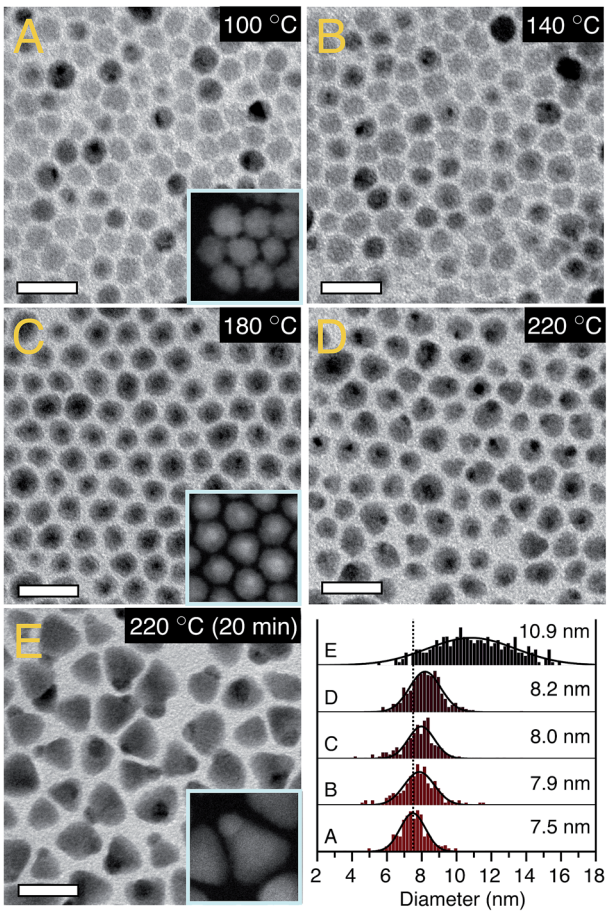

Fig. 2 TEM images of purified aliquots of the reaction mixture during heat-up isolated at (A) 100 °C; (B) 140 °C; (C) 180 °C; (D) 220 °C; (E) 220 °C (20 min). HAADF-STEM images of the corresponding particles are also shown in the insets of (A, C, and E). The particle size distributions (PSDs) are also shown for each of the isolated aliquots. The mean size of each distribution is listed. Scale bars 20 nm.

The observation of mature sized particles at 100 °C is consistent with the high reactivity of the dithiocarbamate precursors used, which are known to decompose readily above 60 °C in the presence of an amine.[50,55,56] This gives rise to rapid nucleation and growth until the metal dithiocarbamate precursors are depleted to equilibrium. Interestingly, the formation of the core/shell structure (which predominantly occurs between 140 °C and 180 °C) takes place with almost no change to the size of the particles. This indicates that the formation of these structures does not occur through a classical route (*i.e.* monomer growth over an existing core) as this would result in larger particles as the shell is formed. Further growth of the particles is only observed at high temperatures, which is attributed to renewed monomer availability through the decomposition of DDT (given it is known to be relatively inactive at temperatures below 200 °C).[57,58] In the later part of the reaction, namely at 220 °C, activation of this secondary sulphur source results in heterogeneous semiconductor (Ag_8GeS_6) deposition onto the existing bulk particle. As such, we observe a massive change in the size of this component while the metal (Ag) protrusion remains relatively constant.

Collectively, the data from Fig. 2 reveal that the formation of the final Janus nanostructure proceeds *via* a complex pathway involving several distinct stages and structural types. To further investigate the products at these stages dark field microscopy was performed. High-angle annular dark field (HAADF) STEM is an ideal means to identify hybrid materials at the nanoscale where differences in material type and density are expected. In this mode, beams scattered at high angles are collected on an annular detector, resulting in atomic number (Z)-contrast. For samples of similar thicknesses (as is the case here due to effectively identical particle sizes) differences in scattered intensity are a direct consequence of the difference in their atomic number. Thus the amorphous carbon support appears black while the particles appear bright. HAADF-STEM images of the particles at key stages during the reaction are shown in the insets of Fig. 2A, C and E. Examination of the image of the initially formed particles (at 100 °C) reveals that their mass distribution is homogeneous. In sharp contrast, by 180 °C the particles have developed a core that is radically different in type and density to the shell material. Given the known identity of

Published on 08 April 2016. Downloaded by Monash University on 5/27/2024 4:09:11 AM.

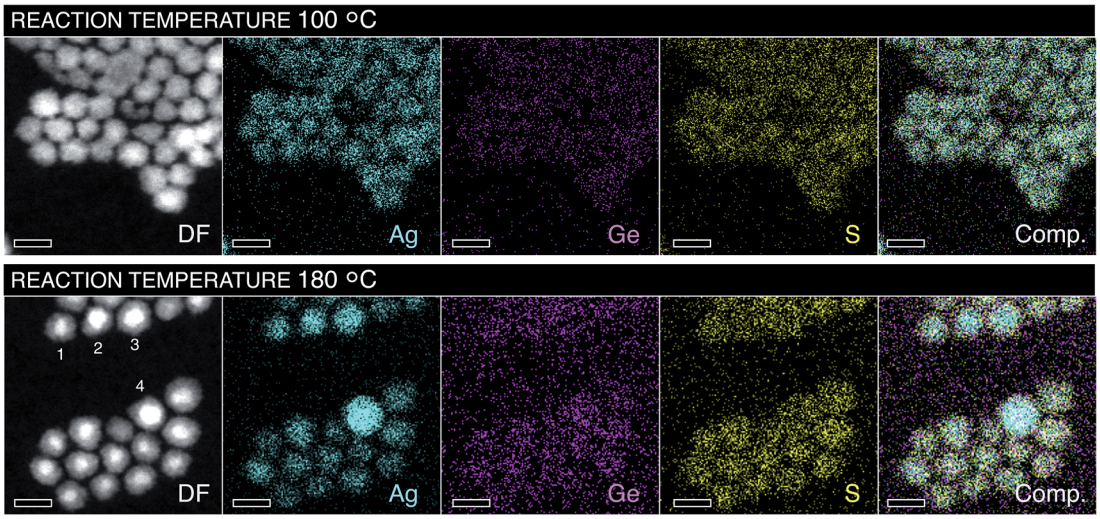

Fig. 3 STEM-XEDS of the initially nucleated particles (at 100 °C) and the core/shell particles (180 °C). From left to right in each row is the dark field STEM image and the subsequent, silver (Ag), germanium (Ge), sulfur (S), and composite (Ag, Ge, S) XEDS maps respectively for the two sets of particles. While the initial particles are seen to be uniform in their elemental composition by 180 °C silver has diffused into the center of the particle giving rise to Ag/Ag_8GeS_6 core/shell heterostructure nanocrystals. Scale bar 10 nm.

the final nanostructure this is strong evidence for an Ag/Ag_8GeS_6 core/shell intermediate. By 220 °C the proposed Ag core component is seen to reside at the vertex/side of the main pyramidal Ag_8GeS_6 crystal.

Given the significant structural changes that occur throughout the reaction, it is important to confirm the identity of the particles at each of these intermediate stages. To accomplish this, elemental analysis using STEM-XEDS was performed. To begin we focus on the transformation of the initially formed particles into the core/shell structure. Fig. 3 shows STEM-XEDS maps of the initially nucleated particles isolated at 100 °C (top panel) and the core/shell particles isolated at 180 °C (lower panel). As previously discussed, in the HAADF image the initially formed particles appear homogeneous in their mass distribution. Analysis of the subsequent elemental maps reveals that the particles contain Ag (cyan), Ge (magenta), and S (yellow) and that all these elements are evenly distributed throughout these particles. This is highlighted in the multicolour composite (Comp.) image of all the detected elements. It is important to note here that the formation of the heterostructures beginning from such nuclei is in sharp contrast to the evolution of other analogous one-pot systems, wherein silver nuclei formed at low temperatures acted as templates for the growth of the semiconductor.[38,47] Given that these systems used only OLA as a solvent, and not a combination of OLA and DDT (as is used here), we postulate that DDT binds silver species in solution, which lowers their supersaturation and prevents their nucleation.§

As expected the HAADF image of the particles at 180 °C shows a core/shell structure. For the purposes of analysis four particles of interest have been labelled with increasing core sizes from 1–4. Inspection of the Ag map immediately reveals that increasing amounts of Ag are present in particles with larger observed cores in the order of 1–4. Similar to the initial particles, germanium and sulphur appear to be quite evenly distributed over the particles. Assuming a core size of 4 nm and a total particle size of 8.5 nm (as predicted from TEM) the shell comprises approximately ten times the volume of the core. In light of this, the observed even distribution of these elements is expected given that on a volume basis the shell will still constitute the dominant XEDS signal from the particle. In spite of this, the presence of Ag rich cores are clearly identifiable. Close examination of particles 1 through 4 in the composite image shows an increasingly larger (cyan coloured) Ag core in direct correlation to the observed core size in the HAADF image. Importantly, the particle is seen to extend beyond the boundaries of the strong Ag signal arising from the core, as exemplified by the clear detection of sulphur in the surrounding region. In conjunction with additional HRTEM data (see ESI; Fig. S2†), HAADF images, and the known identity of the final nanostructure, these data confirm that the core is indeed metallic silver and that the formation of the final Janus structure proceeds *via* an Ag/Ag_8GeS_6 core/shell intermediate.

To explain this phenomenon it is important to recall that the transformation of the initially poorly crystalline silver germanium sulphide nuclei into the Ag/Ag_8GeS_6 core/shell heterostructure occurs predominantly between 140 °C and 180 °C wherein no (statistically relevant) particle growth occurs. As such, the formation of the core/shell structure must occur through the intra-particle diffusion of silver towards the core. As silver is known from numerous examples to be highly diffusive within bulk materials[59,60] (a process that becomes more pronounced in nanocrystals[61–64]) this mechanism of phase separation is not surprising. In fact, silver-based compounds

§ It is important to note here that control reactions conducted by heating the solution to 100 °C in the absence of dithiocarbamate ligand (*i.e.* only Ag and Ge salts in OLA/DDT) did not show the nucleation of any particulate material, proving that Ag nanocrystals could not be produced under these conditions.

 This journal is © The Royal Society of Chemistry 2016

Published on 08 April 2016. Downloaded by Monash University on 5/27/2024 4:09:11 AM.

have been exploited as efficient ion conductors.[65–67] Importantly, HRTEM and XRD data (*vide infra*) prove that the particles formed at 100 °C are poorly or partially crystalline, which would act to facilitate atomic/ionic diffusion within the lattice (see ESI, Fig. S4 and S5† for related HTREM images and electron diffraction data). Assuming that the initial nuclei contain the Ag, Ge, and S elements in a stoichiometry close to Ag_8GeS_6¶, and given that the mean size of the particles is 8.2 nm with an observed mean Ag core size of 3.3 nm, we calculate that only ~14% of the silver would need to diffuse from the surrounding region in order to form the core. Such a small percentage of silver diffusing inward to form the core could be readily accomplished without significantly depleting silver from the outer regions of the particle or requiring additional silver from solution (see ESI, Fig. S3,† for the representative HAADF-TEM image used for analysis).

Clearly, the thermally induced phase separation lowers the total free energy of the system. This process is promoted by three main factors: (i) the high ionic conductivity of the lattice, (ii) the initially poorly crystalline nature of the particles (*vide infra*) that are rich in high-energy defects and grain boundaries, and (iii) the driving force to crystallize the "shell" region.

Having established the mechanism for the initial transformation (from partially crystalline Ag_8GeS_6 to the Ag/Ag_8GeS_6 core/shell) we now focus on the subsequent transformation of these particles into the final Janus nanostructure. In order to gain direct insight into this mechanism *in situ* heating TEM was conducted. To accomplish this the isolated core/shell nanocrystals (extracted from the initial growth solution at 180 °C and then purified) were coated onto a strong carbon coated TEM grid and mounted on a specialized holder that may be used to controllably heat the sample *in situ* within the TEM. In this way we may closely simulate the transformation dynamics that take place in solution and view the effects of temperature on the core/shell nanostructures directly.

The results of this experiment are presented in Fig. 4. Three different particles were examined between temperatures of 100 °C and 300 °C. The structural components of the initial core/shell particle (particle #1) are highlighted by the red (total particle) and green (core only) circles. It can be seen that upon gradually heating the particle from 100–300 °C the Ag core appears to migrate steadily to the particle surface. It is important to note here that given the radically different environments the actual temperature in the TEM can only be loosely correlated to the temperature in solution.[34] Likewise, the effects of the electron beam on the transformation cannot be discounted. Preservation of the spherical shape at high temperatures is expected and rationalized given the absence of available monomer, which precludes the growth of the semiconductor component as occurs in solution. The observation of the core migration to the surface was ubiquitous throughout the sample. Examination of additional particles (particles #2 and #3) reveals

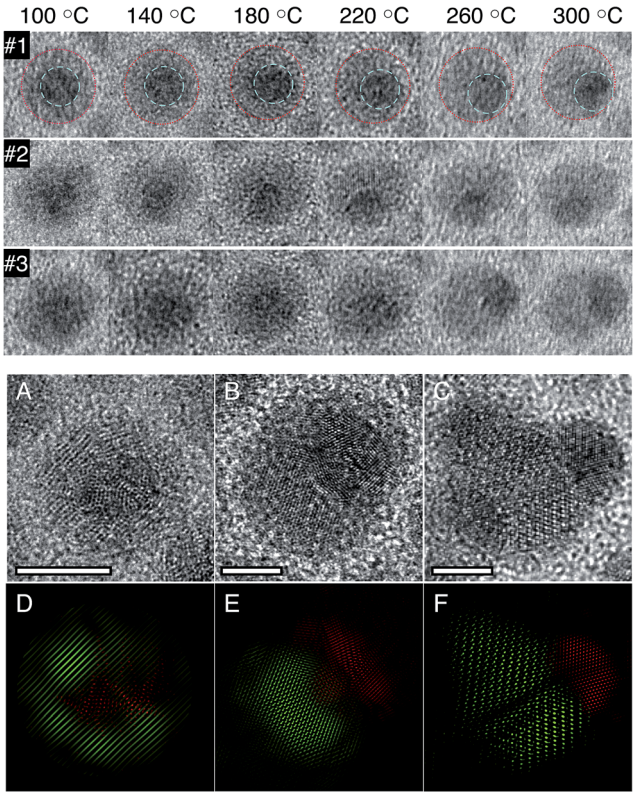

Fig. 4 (Upper panel) HRTEM of three different core/shell structures heated to 300 °C within the electron microscope. The apparent movement (extrusion) of the core to the outside of the particle is clearly visible with increasing temperature. (A–C) HRTEM of selected nanostructures at different stages of exuding the Ag core. (D–F) Corresponding colour coded inverse FFT images (from selected FFT spots) clearly highlighting the Ag (red) and Ag_8GeS_6 (green) components at each stage of the transformation. Scale bars for all images are 5 nm.

the same apparent migration of the Ag-core component to the surface of the nanostructure.

The lower panel of Fig. 4 shows HRTEM images of selected particles representative of the various key stages of transformation into the final Janus nanostructure, specifically: (A) an Ag/Ag_8GeS_6 core/shell structure; (B) a particle with a partially extruded Ag core; (C) the final Janus nanostructure. Image processing is a powerful tool to help uncover the details of complex nanostructured materials. Here we employ a masked FFT analysis to examine the particle more closely during the segregation process. To highlight the exact location of the individual components during segregation, FFT of the HRTEM images was performed and the spots corresponding to either the Ag or Ag_8GeS_6 lattice parameters were selectively masked and inverse FFT images were generated using only the relevant spots. The two images (for each component) were then colour coded and merged to provide the final composite image, which clearly shows the positions of the Ag (red) and Ag_8GeS_6 (green) components at each of these key stages. Although these particles are only examples, they have been carefully chosen to be representative of the general nature of the particles in solution at each of the key stages. Importantly, the initially highly twinned Ag core is visible in Fig. 4 panel A/D.

¶ As established in the later section on XRD the particles are Ag_2S-like. As such, the calculation was also performed for the Ag_2S stoichiometry, which yielded a % atomic diffusion of ~11% from the surrounding regions to form the core.

Published on 08 April 2016. Downloaded by Monash University on 5/27/2024 4:09:11 AM.

Given the observation of thermally induced segregation it is clear that the core/shell structure is not stable at high temperatures. While the initial core/shell structure was formed the resultant Ag–Ag_8GeS_6 interface is clearly observed to be unstable. As the work function of Ag is −4.3 eV [68] and the valence band position of Ag_8GeS_6 is −5.1 eV [49] we expect rapid and efficient electron transfer from the metal to the semiconductor components. This electron transfer would favour an extrusion process by a substitutional interstitial mechanism wherein the Ag^+ ions rapidly diffuse through the lattice to the surface, culminating in the eventual (atom-by-atom) extrusion of the core.[34] In such a case the Ag core would appear to shrink and Ag would begin to appear gradually at the surface. However, from HRTEM and *in situ* heating TEM experiments we know that the core does not change in size during segregation. Given that the core remains intact we safely conclude that the extrusion mechanism is accomplished instead by intra-particle Ostwald ripening of the "shell" onto one side of the core. The drastic difference in crystal structure (large lattice mismatch) between the components results in a high-energy interface between the Ag and Ag_8GeS_6, which favours Ostwald ripening. In order to minimise the surface energy the crystal segregates into a morphology that minimizes the contact area. This is also driven by the (volume) free energy gains of an increasingly well-formed and crystalline Ag_8GeS_6 domain.

From the vantage point of having direct insights into the initial particles, the intermediate core/shell structure and the segregation process, we may now conduct a final investigation into the Janus nanostructure. To unequivocally elucidate the precise elemental composition of the final Janus nanostructure STEM-XEDS spectrum imaging was performed. Fig. 5A shows a bright field (BF)-STEM image highlighting the rectangular region where spectrum imaging was performed. A STEM-XEDS map of a final Janus nanostructure is also provided in the ESI, Fig. S7.† In Fig. 5A the large black box indicates the total scanned area, which contains two individual point-by-point line-scans each containing 43 points. The three coloured boxes indicate the areas over which the multiple XEDS spectra were integrated in order to provide a comprehensive analysis of each individual region. Namely, the Ag_8GeS_6 component (red), Ag component (green), and the background matrix (blue) were all individually assessed. The integrated XEDS spectra are shown in their corresponding colours. Analysis of the metal protrusion is presented in panel B. Peaks from Ag are clearly visible along with peaks arising from the matrix (denoted with star markers). Although tiny peaks at ~1.2 eV and ~2–3 eV corresponding to the expected positions of Ge and S respectively may be seen, these are barely above the background and may be accounted for given the rarity of the beam passing perfectly parallel to the metal–semiconductor interface. In light of this, the spectrum from panel B confirms that only silver metal is present in the protruded component. Conversely, analysis of the bulk component (panel C) shows the presence of all the expected Ag, Ge, and S elements. Collectively, these data prove that Ag core is able to segregate completely to the surface free from any significant contamination from the surrounding Ag_8GeS_6 material.

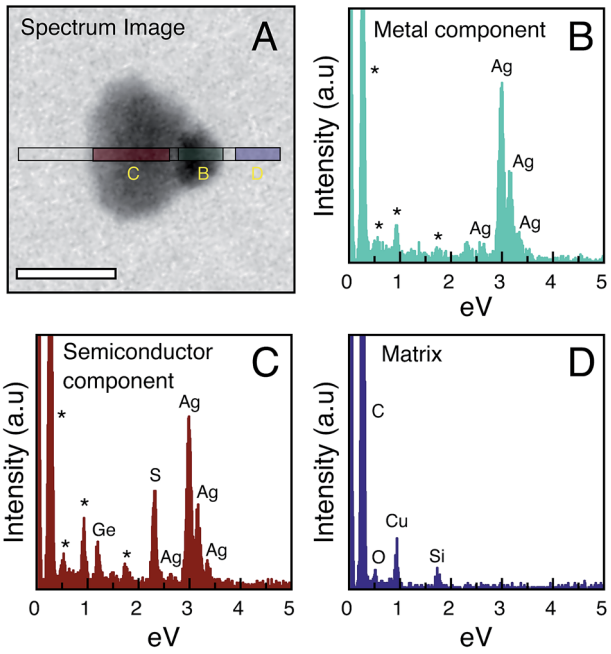

Fig. 5 (A) BF-STEM image showing the rectangular region where STEM-XEDS spectrum imaging was performed over a single typical Janus nanostructure (scale bar 10 nm). Each individually integrated area (from two lines) is highlighted with different colours corresponding to the XEDS spectra for the metal component (B; green), semiconductor component (C; red), and background matrix (D; blue).

With a highly accurate picture of the formation mechanism it is now possible to both adequately interpret and appreciate data from a temperature-dependent XRD analysis. Fig. 6 shows XRD spectra of the reaction solution at different temperatures between 100 °C and 220 °C during the formation of the Janus nanostructures. As all the samples were (relative to the penetration depth of X-rays) effectively of the same thickness the raw data were plotted such that the reader may appreciate changes to the intensity of the reflections, the emergence of various features, as well as the shape of the overall spectra.

To begin, we recall that detailed HRTEM of the initial nuclei at 100 °C revealed partially crystallized (almost amorphous) particles with only small crystalline patches of Ag_8GeS_6 (Fig. S4 and S5†). In support of this HRTEM data, at 100 °C the particles display broad peaks and low signal to noise indicative of a poorly crystalline material. Interestingly, the diffraction pattern corresponds quite well to monoclinic Ag_2S (ICCD 14-0072); shown at the bottom in blue. A detailed view of this spectrum can be found in the ESI (Fig. S6†). The correlation of the 100 °C sample to Ag_2S is somewhat expected given that Ag_2S is known to form at very low temperatures.[69,70] However, from XEDS analysis germanium is known to be present in the particles at early times. Given that the stoichiometric ratio of Ge : Ag in Ag_8GeS_6 is 1 : 8 (~12% Ge) only a slightly lower germanium reaction rate at early times (compared to Ag) would be required to culminate in Ge deficient particles, which would rationalize the appearance of an Ag_2S-like XRD spectrum. As such, it is clear that in spite of the observation of Ag_8GeS_6 patches, the

 This journal is © The Royal Society of Chemistry 2016

Published on 08 April 2016. Downloaded by Monash University on 5/27/2024 4:09:11 AM.

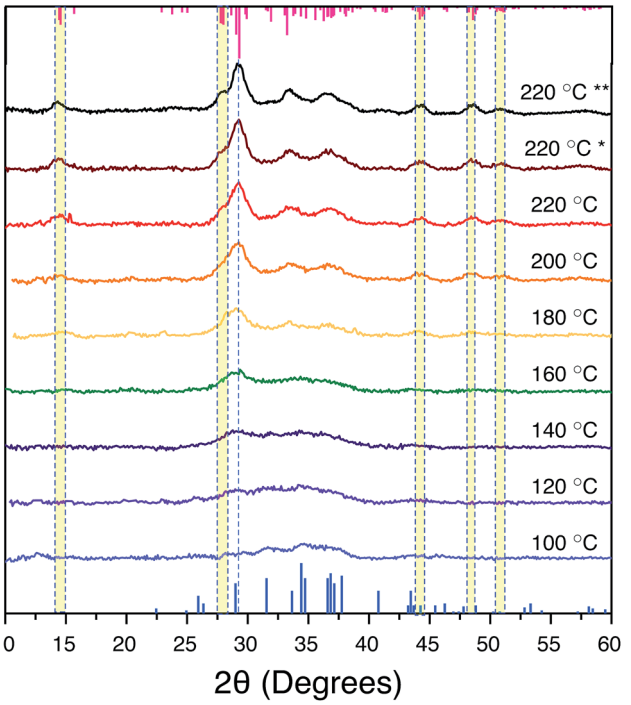

Fig. 6 Temperature dependent XRD data for aliquots of the reaction solution extracted at temperatures between 100 °C and 220 °C. The initial particles at 100 °C are poorly crystalline and are Ag_2S-like. The particles are seen to become increasingly crystalline and display clear Ag_8GeS_6 peaks. *10 min growth and **20 min growth.

predominant "amorphous" sections of the particle are Ag_2S-like and give rise to an XRD pattern well matched to the Ag_2S phase.

As the reaction is heated the initial poorly crystalline sample begins to adopt a pattern indicative of Ag_8GeS_6 (expected XRD pattern shown at the top in pink). This transformation is seen through the gradual emergence of the main [002] reflection of Ag_8GeS_6 at ~29.2° (dashed blue line) as the sample is heated from 100–220 °C. Furthermore, additional diffraction regions unique to Ag_8GeS_6 (as opposed to Ag_2S) are seen to appear concomitantly with the increasing intensity of the [002] reflection (yellow shaded regions).

Importantly, the sample is seen to remain quite poorly crystalline up until 180 °C, which is coincident with the stage wherein formation of the core/shell structure occurs through Ag diffusion. Not surprisingly, crystallization is inhibited during the thermally induced phase separation stage of the reaction. However, by ~180 °C the core/shell structure begins to show features more consistent with Ag_8GeS_6 (clusters of reflections around 14, 43, 46, and 51°) and generally appears quite crystalline considering that the Ag_8GeS_6 shell is only ~2–3 nm thick. The higher temperature coupled with the full segregation of the Ag core (220 °C*), facilitates and permits improved crystallization of the semiconductor Ag_8GeS_6 component, which is corroborated by both the HRTEM analysis and further sharpening of the peaks in the XRD patterns. Additional heating at 220 °C (*i.e.* after full segregation) results in only marginal improvement to the overall crystallinity of the sample.

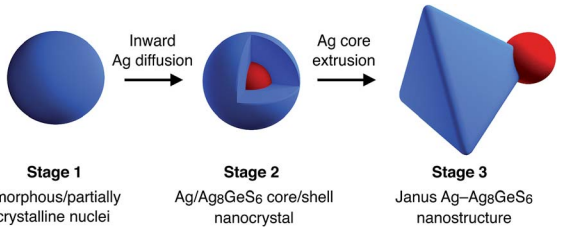

Scheme 1 Schematic of the three main stages of transformation that occur during the formation of Janus Ag–Ag_8GeS_6 nanostructures.

Through extensive analysis using HRTEM, HAADF-STEM, XEDS mapping, *in situ* heating in the TEM, and XRD we have uncovered the complete formation mechanism of the Ag–Ag_8GeS_6 Janus nanostructures. Scheme 1 summarizes these findings and the key stages of the dynamic processes involved.

It is now clear that the final Ag–Ag_8GeS_6 Janus nanostructures are formed in three distinct stages: (i) nucleation of nearly amorphous defect-rich silver germanium sulphide nuclei, which have just begun to partially crystallize the Ag_8GeS_6 phase; (ii) thermally induced phase separation into an Ag/Ag_8GeS_6 core/shell heterostructure by inward Ag diffusion; (iii) intra-particle Ostwald ripening resulting in extrusion of the Ag-core to the surface and the full crystallization of the final resultant Janus Ag–Ag_8GeS_6 nanostructure.

Optical data

To investigate the optical changes during the formation of the Ag–Ag_8GeS_6 nanostructures aliquots were taken from the reaction solution at different temperature intervals during the heat-up process. Each of these aliquots was of a known mass and diluted with the same amount of solvent. As such, by correcting for the dilution factor the effective absorbance profile of the nanostructures within the reaction solution may be examined directly.

Fig. 7 shows the absorbance spectra at key intervals during heat-up between 100 °C and 220 °C. Inspection of Fig. 7 reveals that while the absorbance at higher energies remains relatively constant the band edge shifts progressively to higher energies as the solution is heated. The initial spectrum at 100 °C has a slow onset at a similar energy to that of Ag_2S (~1200 nm) and is consistent with the aforementioned XRD data that these initial particles are poorly crystalline and Ag_2S-like. The subsequent blue-shift of the absorbance spectra with heating is indicative of possible continued germanium incorporation and the slow segregation and crystallization of the Ag_8GeS_6 component. Notably, little change is observed in the absorbance spectra once the formation of the nanostructure is complete, despite the fact that further growth of the semiconductor component at 220 °C is known to occur.

The drastic changes to the electronic structure are best observed from Tauc plot analysis (Fig. 7B and C). Such analysis is useful to indicate whether the band profile has more direct or indirect character. The initial particles are seen to have a strongly indirect character with a band gap at ~0.9 eV. Both the energy and dominant indirect character off the band profile

Published on 08 April 2016. Downloaded by Monash University on 5/27/2024 4:09:11 AM.

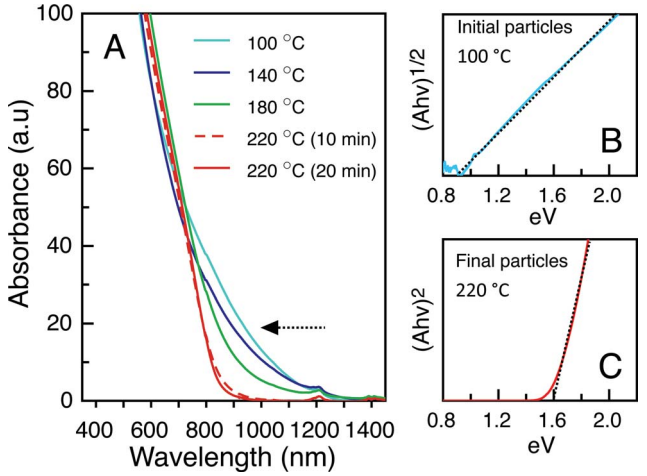

Fig. 7 (A) Corrected absorbance spectra taken from aliquots of the reaction solution as it is heated from 100 °C to 220 °C during the formation of the Ag–Ag_8GeS_6 nanostructure. (B) Tauc plot showing the indirect character of the initial particles. (C) Tauc plot showing the direct character of the final Janus nanostructures.

is consistent with poorly crystalline Ag_2S-like nuclei. The poorly crystalline nature of the initially nucleated particles gives rise to defects both within and at the surface of the particles and contributed indirect character to the band profile. Upon segregation and full crystallization (defect annealing) the band profile better reflects that of the bulk Ag_8GeS_6 component, which changes to a more direct band gap at 1.6 eV at the conclusion of the reaction.‖ Previous investigations on pure Ag_8GeS_6 nanocrystals revealed a band gap of ~1.45 eV.[49] While the difference between these values is minimal, we cannot rule out that the high electron density at the metal–semiconductor interface perturbs the optical properties and results in a slightly higher band gap within the more complex Ag–Ag_8GeS_6 nanostructure.

Conclusions

The heat-up synthetic method used here permits the production of large quantities of nanomaterials as required to efficiently evaluate these nanostructures in energy-based and catalytic applications. Through the use of highly reactive silver and germanium sources, coupled with the careful optimization of the ligand chemistry, we have successfully synthesised Janus Ag–Ag_8GeS_6 nanostructures in a single step "one-pot" reaction. By terminating the reaction at different temperatures the reaction scheme outlined here can be used to generate large quantities of novel highly monodisperse Ag/Ag_8GeS_6 core/shell nanocrystals, as well as Ag–Ag_8GeS_6 heteronanostructures.

‖ To better understand the optoelectronic properties of the dominant Ag_8GeS_6 component its electronic structure was modelled using first principles methods with generalized gradient approximation (GGA) and HSE06 functional. These simulations yielded a band gap of ~1.79 eV, slightly larger than the experimentally observed band gap of 1.60 eV. A more in depth analysis of the first principles simulations is provided in the ESI (Fig. S8†).

By employing a suite of analytic techniques we have successfully decoupled the dynamic transformation mechanisms that lead to the formation of the final Ag–Ag_8GeS_6 Janus nanostructures. The insights gained provide a deeper understanding of the mechanisms required to effect such phase separations and transformations in non-injection reactions.

Utilizing highly reactive silver, sulphur, and germanium precursors, as well as a strongly capping ligand (DDT), the formation of template silver nuclei, common to other systems, was circumvented. Instead the reaction was determined to proceed through (germanium containing) Ag_2S-like nuclei. Relying on the facile phase separation of silver, template nuclei of this kind could be doped with other elements besides germanium (provided their precursors are quite highly reactive). As such, the method described here provides a rational design strategy to generate more complex ternary and quaternary Ag-semiconductor heterostructures with tailored optical and electrical properties.

Acknowledgements

J. v. E. and E. D. G. acknowledge funding from the Office of the Chief Executive through the CSIRO Manufacturing Flagship. J. v. E., A. S. R. C., and J. J. J. acknowledge the Australian Research Council for funding through grants DE150100427, DE130100635, and DP110105341, respectively. Y. Y. and N. V. M. acknowledge the computational support from the National Computing Infrastructure and Pawsey Supercomputing Centre funded by the Government of Australia. L. B. acknowledges the use of facilities within the Monash Centre for Electron Microscopy.

Notes and references

1 X. Y. Ling, I. Y. Phang, C. Acikgoz, M. D. Yilmaz, M. A. Hempenius, G. J. Vancso and J. Huskens, *Angew. Chem.*, 2009, **121**, 7813–7818.
2 C. de Mello Donega, *Chem. Soc. Rev.*, 2011, **40**, 1512–1546.
3 L. Carbone and P. D. Cozzoli, *Nano Today*, 2010, **5**, 449–493.
4 H. Liu, Y. Feng, D. Chen, C. Li, P. Cui and J. Yang, *J. Mater. Chem. A*, 2015, **3**, 3182–3223.
5 M. Lattuada and T. A. Hatton, *Nano Today*, 2011, **6**, 286–308.
6 R. Jiang, B. Li, C. Fang and J. Wang, *Adv. Mater.*, 2014, **26**, 5274–5309.
7 A. Kudo and Y. Miseki, *Chem. Soc. Rev.*, 2009, **38**, 253–278.
8 A. Vaneski, A. S. Susha, J. Rodríguez-Fernández, M. Berr, F. Jäckel, J. Feldmann and A. L. Rogach, *Adv. Funct. Mater.*, 2011, **21**, 1547–1556.
9 R. Costi, A. E. Saunders, E. Elmalem, A. Salant and U. Banin, *Nano Lett.*, 2008, **8**, 637–641.
10 J. Yang and J. Y. Ying, *Angew. Chem., Int. Ed.*, 2011, **50**, 4637–4643.
11 C. Wang, H. Daimon and S. Sun, *Nano Lett.*, 2009, **9**, 1493–1496.
12 R. Lavieville, Y. Zhang, A. Casu, A. Genovese, L. Manna, E. Di Fabrizio and R. Krahne, *ACS Nano*, 2012, **6**, 2940–2947.

This journal is © The Royal Society of Chemistry 2016

Published on 08 April 2016. Downloaded by Monash University on 5/27/2024 4:09:11 AM.

13 M. Meyns, S. Willing, H. Lehmann and C. Klinke, *ACS Nano*, 2015, **9**, 6077–6087.
14 U. Banin, Y. Ben-Shahar and K. Vinokurov, *Chem. Mater.*, 2014, **26**, 97–110.
15 H. Yu, M. Chen, P. M. Rice, S. X. Wang, R. L. White and S. Sun, *Nano Lett.*, 2005, **5**, 379–382.
16 H. Yin, C. Wang, H. Zhu, S. H. Overbury, S. Sun and S. Dai, *Chem. Commun.*, 2008, 4357–4359.
17 S. Liang, X. L. Liu, Y. Z. Yang, Y. L. Wang, J. H. Wang, Z. J. Yang, L. B. Wang, S. F. Jia, X. F. Yu, L. Zhou, J. B. Wang, J. Zeng, Q. Q. Wang and Z. Zhang, *Nano Lett.*, 2012, **12**, 5281–5286.
18 D. Grodzińska, F. Pietra, M. A. van Huis, D. Vanmaekelbergh and C. de Mello Donegá, *J. Mater. Chem.*, 2011, **21**, 11556–11565.
19 I. R. Franchini, G. Bertoni, A. Falqui, C. Giannini, L. W. Wang and L. Manna, *J. Mater. Chem.*, 2010, **20**, 1357–1366.
20 C. D. M. Donegá, *Chem. Soc. Rev.*, 2011, **40**, 1512–1546.
21 A. Perro, S. Reculusa, S. Ravaine, E. Bourgeat-Lami and E. Duguet, *J. Mater. Chem.*, 2005, **15**, 3745–3760.
22 Y. Wang, T. Ding, J. J. Baumberg and S. K. Smoukov, *Nanoscale*, 2015, **7**, 10344–10349.
23 C. Zhu, J. Zeng, J. Tao, M. C. Johnson, I. Schmidt-Krey, L. Blubaugh, Y. Zhu, Z. Gu and Y. Xia, *J. Am. Chem. Soc.*, 2012, **134**, 15822–15831.
24 J. He, M. T. Perez, P. Zhang, Y. Liu, T. Babu, J. Gong and Z. Nie, *J. Am. Chem. Soc.*, 2012, **134**, 3639–3642.
25 D. Rodríguez-Fernández and L. M. Liz-Marzán, *Part. Part. Syst. Charact.*, 2013, **30**, 46–60.
26 E. A. Hernández-Pagán, A. D. P. Leach, J. M. Rhodes, S. Sarkar and J. E. Macdonald, *Chem. Mater.*, 2015, **27**, 7969–7976.
27 X. Yu, X. An, A. Genç, M. Ibáñez, J. Arbiol, Y. Zhang and A. Cabot, *J. Phys. Chem. C*, 2015, **119**, 21882–21888.
28 I. R. Franchini, G. Bertoni, A. Falqui, C. Giannini, L. W. Wang and L. Manna, *J. Mater. Chem.*, 2010, **20**, 1357–1366.
29 T. R. Gordon and R. E. Schaak, *Chem. Mater.*, 2014, **26**, 5900–5904.
30 T. Mokari, E. Rothenberg, I. Popov, R. Costi and U. Banin, *Science*, 2004, **304**, 1787–1790.
31 H. Gu, Z. Yang, J. Gao, C. K. Chang and B. Xu, *J. Am. Chem. Soc.*, 2005, **127**, 34–35.
32 S. Liang, X. L. Liu, Y. Z. Yang, Y. L. Wang, J. H. Wang, Z. J. Yang, L. B. Wang, S. F. Jia, X. F. Yu, L. Zhou, J. B. Wang, J. Zeng, Q. Q. Wang and Z. Zhang, *Nano Lett.*, 2012, **12**, 5281–5286.
33 P.-J. Wu, J.-W. Yu, H.-J. Chao and J.-Y. Chang, *Chem. Mater.*, 2014, **26**, 3485–3494.
34 J. Yang and J. Y. Ying, *J. Am. Chem. Soc.*, 2010, **132**, 2114–2115.
35 S. K. Han, C. Gu, M. Gong, Z. M. Wang and S. H. Yu, *Small*, 2013, **9**, 3765–3769.
36 M. Pang, J. Hu and H. C. Zeng, *J. Am. Chem. Soc.*, 2010, **132**, 10771–10785.
37 J. Zhou, F. Huang, J. Xu and Y. Wang, *Chem.–Asian J.*, 2014, **9**, 3287–3290.
38 F. Jiang, Q. Tian, M. Tang, Z. Chen, J. Yang and J. Hu, *CrystEngComm*, 2011, **13**, 7189–7193.
39 S. K. Han, M. Gong, H. B. Yao, Z. M. Wang and S. H. Yu, *Angew. Chem., Int. Ed.*, 2012, **51**, 6365–6368.
40 H. Ye, A. Tang, L. Huang, Y. Wang, C. Yang, Y. Hou, H. Peng, F. Zhang and F. Teng, *Langmuir*, 2013, **29**, 8728–8735.
41 Y. Zhang, S. Shen and Q. Wang, *CrystEngComm*, 2014, **16**, 9501–9505.
42 S. Shen, Y. Zhang, Y. Liu, L. Peng, X. Chen and Q. Wang, *Chem. Mater.*, 2012, **24**, 2407–2413.
43 S. Shen, Y. Zhang, L. Peng, Y. Du and Q. Wang, *Angew. Chem., Int. Ed.*, 2011, **50**, 7115–7118.
44 S.-U. Lee, J. W. Hong, S.-I. Choi and S. W. Han, *J. Am. Chem. Soc.*, 2014, **136**, 5221–5224.
45 B. Liu and Z. Ma, *Small*, 2011, **7**, 1587–1592.
46 S. Xiong, B. Xi, K. Zhang, Y. Chen, J. Jiang, J. Hu and H. C. Zeng, *Sci. Rep.*, 2013, **3**, 2177.
47 Q. He, S. Huang, C. Wang, Q. Qiao, N. Liang, M. Xu, W. Chen, J. Zai and X. Qian, *ChemSusChem*, 2015, **8**, 817–820.
48 Q. He, T. Qian, J. Zai, Q. Qiao, S. Huang, Y. Li and M. Wang, *J. Mater. Chem. A*, 2015, **3**, 20359–20365.
49 B. Zhou, Y. Xing, S. Miao, M. Li, W.-H. Zhang and C. Li, *Chem.–Eur. J.*, 2014, **20**, 12426–12431.
50 A. S. R. Chesman, J. van Embden, E. Della Gaspera, N. W. Duffy, N. A. S. Webster and J. J. Jasieniak, *Chem. Mater.*, 2014, **26**, 5482–5491.
51 A. S. R. Chesman, J. van Embden, N. W. Duffy, N. A. S. Webster and J. J. Jasieniak, *Cryst. Growth Des.*, 2013, **13**, 1712–1720.
52 J. van Embden, A. S. R. Chesman and J. J. Jasieniak, *Chem. Mater.*, 2015, **27**, 2246–2285.
53 D. Aherne, D. M. Ledwith, M. Gara and J. M. Kelly, *Adv. Funct. Mater.*, 2008, **18**, 2005–2016.
54 T. C. R. Rocha and D. Zanchet, *J. Phys. Chem. C*, 2007, **111**, 6989–6993.
55 Y. K. Jung, J. I. Kim and J. K. Lee, *J. Am. Chem. Soc.*, 2010, **132**, 178–184.
56 N. Pradhan, B. Katz and S. Efrima, *J. Phys. Chem. B*, 2003, **107**, 13843–13854.
57 Z. Zhuang, X. Lu, Q. Peng and Y. Li, *Chem.–Eur. J.*, 2011, **17**, 10445–10452.
58 A. S. R. Chesman, N. W. Duffy, S. Peacock, L. Waddington, N. A. S. Webster and J. J. Jasieniak, *RSC Adv.*, 2013, **3**, 1017–1020.
59 B. F. Dyson, *J. Appl. Phys.*, 1966, **37**, 2375–2377.
60 H. E. Cook and J. E. Hilliard, *J. Appl. Phys.*, 1969, **40**, 2191–2198.
61 S. Schumacher, R. Birringer, R. Strauß and H. Gleiter, *Acta Metall.*, 1989, **37**, 2485–2488.
62 J. Horváth, R. Birringer and H. Gleiter, *Solid State Commun.*, 1987, **62**, 319–322.
63 H. S. Dong, S. M. Hughes, Y. Yin and A. P. Alivisatos, *Science*, 2004, **306**, 1009–1012.
64 G. Prusty, A. K. Guria, B. K. Patra and N. Pradhan, *J. Phys. Chem. Lett.*, 2015, **6**, 2421–2426.

65 V. M. Nield, D. A. Keen, W. Hayes and R. L. McGreevy, *Solid State Ionics*, 1993, **66**, 247–258.
66 M. H. Hebb, *J. Chem. Phys.*, 1952, **20**, 185–190.
67 Z. Xu, Y. Bando, W. Wang, X. Bai and D. Golberg, *ACS Nano*, 2010, **4**, 2515–2522.
68 D. E. Eastman, *Phys. Rev. B: Solid State*, 1970, **2**, 1–2.
69 Y. Zhang, Y. Liu, C. Li, X. Chen and Q. Wang, *J. Phys. Chem. C*, 2014, **118**, 4918–4923.
70 W. Lou, X. Wang, M. Chen, W. Liu and J. Hao, *Nanotechnology*, 2008, **19**, 225607.
71 T. R. Anantharaman and C. Suryanarayana, *J. Mater. Sci.*, 1971, **6**, 1111–1135.

Published on 08 April 2016. Downloaded by Monash University on 5/27/2024 4:09:11 AM.

This journal is © The Royal Society of Chemistry 2016